

## 10A-02 HOW HIGH THE RESOLUTION CAN WE REFER FOR THE X-BAND RADAR PRECIPITATION MEASUREMENT IN URBAN REGIONS

Yaoyao Zheng\*, Jan Handwerker, Norbert Kalthoff  
 Karlsruhe Institute of Technology, Karlsruhe, Germany

### 1. INTRODUCTION

Radar-based quantitative precipitation estimates (QPE) have been used as input data to hydrologic models for flooding forecast. The precipitation data for hydrologic applications should be high-resolution, particularly for the small-size catchments and urban regions. The national operational radar network of German Weather Service provides precipitation measurements at 500-meter resolution. Such resolution maybe too coarse for hydrologic modeling and also might not be able to capture the characteristics of convective precipitation systems. Thus, higher spatial resolution could be intuitively a better option. However, we have no concrete evidence about whether our radar measurement can obtain more useful or unwanted information by introducing higher spatial resolutions.

X-band radar is portable when comparing to C-band or S-band counterparts, allowing us to situate the X-band radar closer to the region of our interest. However, attenuation issue limits the usage of X-band radar data for QPE. For past decades, the dual-polarization quantities have been used to mitigate the attenuation issue for X-band radars' measurements. Dual-polarization data also provide additional information about the precipitation. Therefore, we are also interested in how the higher spatial resolutions affect the usage of dual-polarization quantities for applications such as discriminating meteorological and non-meteorological echoes.

To understand whether the high resolution can bring more useful information, and whether the high resolution can improve the performance of applying radar data in the precipitation estimation can help us to determine the spatial resolution for radar measurement. As follows, we will briefly introduce our radar experiment and data, and then compare radar data in different spatial resolutions in terms of their data quality, QPE and other applications including filtering non-meteorological echoes, tracking convective storms and hail detection.

### 2. EXPERIMENT AND DATA

The Meteor 50DX (Selex Systems Integration GmbH) dual-polarized X-band radar was operated at 48.8°N, 9.25°E near the city of Stuttgart in Germany from May 23-October 17 in 2017. Stuttgart metropolitan region is one of largest populated urban areas in Germany and is characterized by complex topographic features. During this field experiment, our X-band radar was operated with two spatial resolutions alternatively. For each 10-minute time span, the 'fine scan' with 75m radial resolution was repeated three times, followed by one 'coarse scan' with 250m radial resolution. In this way, we can regard

the alternative fine scan and coarse scans within each 10-minute period as quasi-simultaneous. Due to the local administration on microwave, there was no radar measurement in the sector between the azimuths of 91°-170°, as shown in Fig. 1. Other technical details can be found in the table 1. In order to focus on the effect of resolution exclusively, we try to control other aspects of fine scan and coarse scan as similar as possible. For instance, we constrain our investigation to the range coverage within 75km in radius to eliminate the range effect caused by the additional coverage from 75km to 100km in radius for the coarse scan.

**Table 1.** Performance parameters for the X-band radar measurements

Scan name	Fine	Coarse
Range resolution (m)	75	250
Operation range (km)	75	100
Pulse repetition frequency (Hz)	2000	500
Pulse width (μs)	0.5	2
Scan duration (seconds)	100	255
Volume elevations (°)	1.5, 3.2, 5.0 (before 13:30 UTC June 6, 2017); 1.5, 3.0, 6.2 (After 13:30 UTC June 6, 2017)	1.5, 3.6, 6.2, 9.4, 13.3, 18, 23.8, 30.8, 39.5, 90
Antenna speed (°/s)	13.5	18
Azimuthal resolution (°)	1.3	

Our X-band radar data includes measurements of radar reflectivity ( $Z_H$ ), differential radar reflectivity ( $Z_{DR}$ ), total differential phase shift ( $\Phi_{DP}$ ), specific differential phase ( $K_{DP}$ ), copolar correlation coefficient ( $\rho_{HV}$ ), signal-to-noise ratio (SNR), signal quality index (SQI), and clutter correction ratio (CCOR). For the quantitative precipitation estimation, we apply the Marsh-Palmer Z-R relation ( $Z_H = 200 R^{0.6}$ ) or the specific differential phase ( $K_{DP}$ )-based rainfall estimator ( $R = 17 K_{DP}^{0.73}$ ) both scans to estimate the precipitation quantitatively. Interpolation or average of radar reflectivity will be performed in the unit of rainfall rate by converting the radar reflectivity to the rainfall rate using the Marsh-Palmer relation. Radial texture parameters for  $Z_H$ ,  $Z_{DR}$ ,  $\Phi_{DP}$  and  $\rho_{HV}$  is also calculated with the moving 1-km radial window, which means a radial window in length of 5 gates for the coarse scan and 15 gates for the fine scan.

\* Corresponding author address: Yaoyao Zheng, Karlsruhe Institute of Technology, Institute for Meteorology and Climate Research, 76344 Eggenstein-Leopoldshafen, Germany; e-mail:

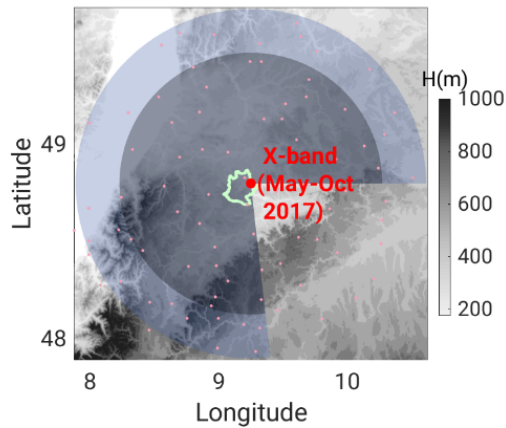


Figure 1 illustrates the X-band radar experiment, where the light green curve is the boundary of Stuttgart city, and the red dot is the location of X-band radar, and the small pink dots indicate the rain gauge network of German Weather Service with the X-band radar coverage.

Besides the X-band radar data, 1-minute precipitation measurement from German Weather Service (DWD) rain gauge network as displayed in Fig.1 is also involved as the reference measurement for the surface precipitation.

### 3. DATA QUALITY AND DATA ASSURANCE

#### 3.1 Noise Filtering

Fig. 2 shows the accumulated precipitation (AR) amount estimated from radar reflectivity ( $Z$ ) of both fine scan and coarse scan for a fixed 5-hour period. It is apparent that the fine scan retrieves much more precipitation amount than that of coarse scan. According to surface precipitation measurements from rain gauge network, this period should be nearly dry within our radar coverage. Thus, the fine scan produces 'fake' precipitation attributed to the noise in fine scan. To eliminate the noise that is more prevalent in the fine scan, a filtering with threshold of SQI of 0.3 is applied exclusively to the fine scan data and most of the 'fake' precipitation is removed thereafter (seen in Fig.2).

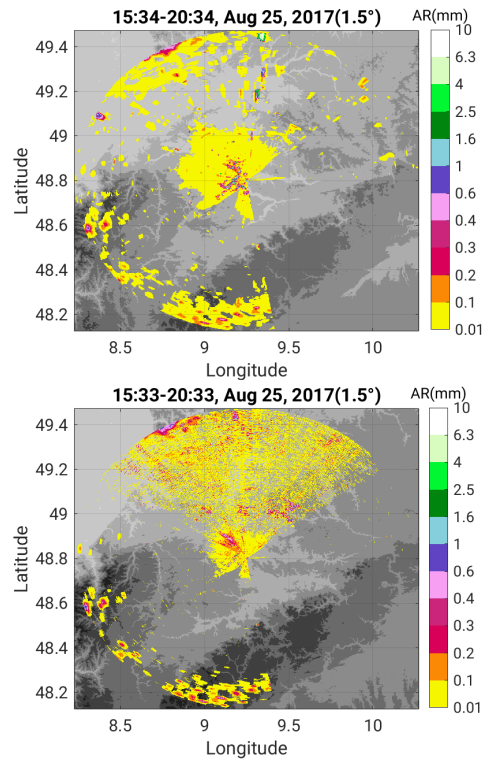
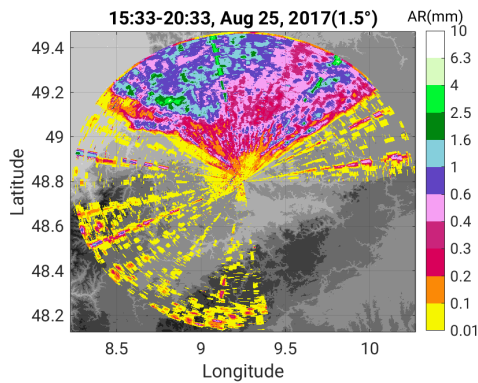
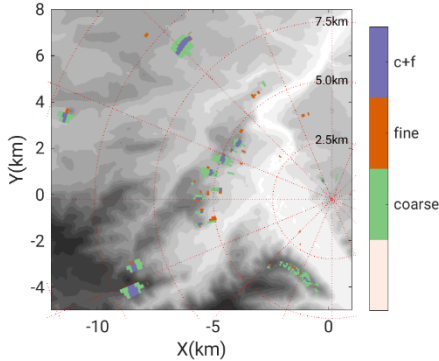


Figure 2 shows Radar reflectivity ( $Z_H$ )-based accumulated precipitation amount during 15:30-20:30 UTC on August 25, 2017 (top: fine scan, middle: coarse scan, bottom: fine scan after filtering noise).

#### 3.2 Static Ground Clutter Identification

The static ground clutter mapping based on the data availability of radar reflectivity above 35dBZ at the lowest elevation is established respectively for both fine and coarse scan. If more than 1% of data is above 35dBZ, then that gate will be identified as static ground clutter (SGC). As shown in the Fig. 3, the majority of SGC gates lie reasonably along the topographic ridges. By comparing the SGC identification from both fine and coarse scans, we notice two differences. The first difference is that the fine scan data identify a smaller area of SGC compared to the coarse scan, and the second difference is that a few isolated gates are identified solely by fine scan. The reason for the first difference is that the individual resolution volume or scattering volume of fine scan is smaller and hence can better represent the subtle spatial structure of the ground clutters. In contrast, the resolution volume of coarse scan is roughly three times larger than that of fine scan at the same location, and it contains the information that is equivalent to the average of three resolution volumes of fine scan in proximity. Given that three consecutive gates named as G1, G2 and G3 in fine scan are equivalent to one gate named as G0 in the coarse scan, for instance, if only G2 contains ground clutter, averaging over these three gates reduces the probability of agglomeration of G1, G2 and G3 to be identified as SGC, which explains the second difference aforementioned. Another scenario is that both G1 and G2 contain ground clutters, and G0 is also identified as SGC, but G3 does not contain ground clutter. The normal

procedure after the identification of static ground clutter (SGC) is to exclude these SGC gates in the subsequent quantitative precipitation estimation. So, we cannot retrieve the precipitation estimation for the area of G3 that does not contain ground clutter but is wrongly identified as SGC by the coarse scan.



**Fig. 3** Mapping of static ground clutter (SGC) for both fine scan and coarse scan, where the purple gates are identified both by coarse and fine scans, the orange gates are only identified by the fine scan, and the green gates are only identified by the coarse scan

### 3.3 Non-Precipitating Echo Identification

In our experiment, precipitation echoes in the lowest two elevations are contaminated by the non-meteorological echoes. Insects are the main source of the biological scatters in this study because our experiment was performed in the summer time. Our radar is located northeast only 5-km away from the city center that is in a basin surrounded by the hills, so ground clutters exist in the southwestern direction of the radar coverage.

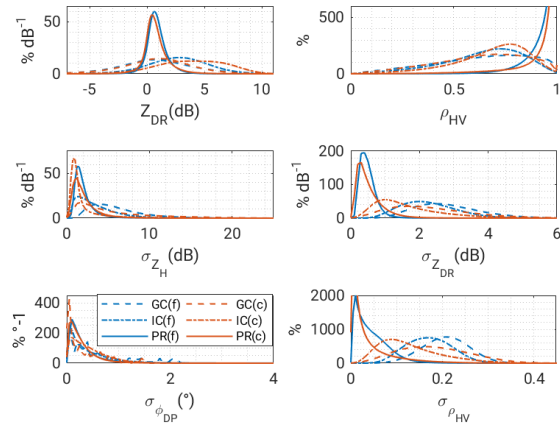


**Fig. 4** Probability density distribution of differential radar reflectivity ( $Z_{DR}$ ), copular correlation coefficient ( $\rho_{HV}$ ) and the radial texture for radar reflectivity ( $Z_H$ ),  $Z_{DR}$ , total differential phase shift ( $\Phi_{DP}$ ) and  $\rho_{HV}$  for ground clutter (GC), insect clutter (IC) and precipitation (PR) for fine and coarse scan respectively

Before filtering out the non-precipitating echoes, the characteristics of ground clutter (GC), biologic scatter, mainly insect (IC) and precipitation (PR) echoes are described by the probability density distribution of dual-polarization quantities and their radial texture parameters shown in Fig. 4. To clarify,

the ground clutters discussed herein include both static and dynamic ground clutters, and anomalous propagation. Differing from Dufton (2017), noise class is not discussed separately because the majority of noise in fine scan has been removed by the SQL filtering in session 3.2. Echoes of three classes are identified by expert inspection. To guarantee the representativeness of three classes to mitigate the subjectivity, we use a large number of volume scans (seen Table 2) as training data and these volume scans are selected deliberately from different meteorological conditions both daytime and nighttime from May to October. Contamination of ground clutter and insect usually occurs near the radar and below 1km above the ground surface, so only the range gates with 25km away from the radar are considered for ground clutters and biologic scatters. Since some ground clutters are persistent, the insect echoes are inevitably mixed with the ground clutter. Thus, a static ground clutter map shown in Fig 3, as discussed in session 3.2 is used to remove the spurious gates contaminated by the long-residing ground clutters. Moreover, precipitation echoes within the radar coverage of 25km in radius are excluded in order to get rid of the contamination from ground clutter and biologic scatters.

**Table 2.** Number of volume scans used to establish the training database for discriminating three classes of echoes

Type of echo	Fine scan	Coarse scan
Ground clutter (GC)	830	275
Insect clutter (IC)	2000	650
Precipitation (PR)	770	260

As indicated in Fig. 4, three classes of echoes (GC, IC and PR) exhibit different probability density distribution especially in terms of the quantities  $\rho_{HV}$ , the radial texture parameters of  $\rho_{HV}$  and  $Z_{DR}$ . Precipitation echoes are characterized by high copular correlation coefficients, and low radial texture parameters for  $Z_{DR}$  and  $\rho_{HV}$ . The texture parameter of total differential phase shift ( $\Phi_{DP}$ ) reveals show inability to distinguish the precipitation and insect echoes, which is in contradictory to their usage used in the fuzzy logic classification (Park et al, 2008; Dufton et al, 2015).

Furthermore, the probability density distributions from fine scan and coarse scan also differ. For both texture of  $Z_{DR}$  and  $\rho_{HV}$ , the insect class has smaller textures for fine scan than those of coarse scan. In other words, the fine scan data provides a smaller overlap between the precipitation echoes and the insect echoes. In the fuzzy logic identification between precipitating echoes and non-precipitating echoes, membership functions seen in Fig. 5 are usually established based on the probability distribution. If we apply the identical membership functions to both fine scan and coarse scan, a smaller overlap, available in fine scan data, between the insect echoes and precipitation echoes indicates less probability of false or missing identification.

Fig. 5 shows that fine scan provides a larger texture of  $\rho_{HV}$  for non-precipitating echoes. In the previous calculation of radial texture parameters, we use the moving window of the same length for both

scans which implies that the calculation of radial texture for fine scan involves three times more gates than that of the coarse scan. Thus, one possible explanation for the larger texture of  $\rho_{HV}$  obtained from fine scan is that non-precipitating echoes exhibit a notably fluctuating nature, which is better kept on the condition of a finer spatial resolution.

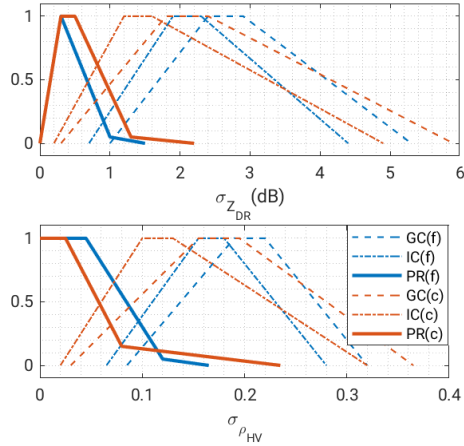


**Fig. 5** Trapezoidal or triangle membership function for ground clutter (GC), insect clutter (IC), and precipitation (PR) for fine scan and coarse scan respectively

### 3.4 Sensitivity to Attenuation Correction

X-band radar measurement suffers serious attenuation issue due to its short wavelength. The iterative ZPHI method (Gematronik, 2007) is used to correct the radar reflectivity and the specific attenuation of horizontal reflectivity-scale method (Gematronik, 2007) is applied to correct the differential radar reflectivity for both fine and coarse scans in this study. These attenuation correction methods primarily rely on the total differential phase shift ( $\Phi_{DP}$ ), which is a variable integrating through the entire propagation path and theoretically should not be affected by the radial resolution of the resolution volume. However, data masking and iterative filtering (Gematronik, 2007), which is always required before using  $\Phi_{DP}$ , might be affected by the resolution of the data. As illustrated in Fig. 6, between 50km-60km along the range, the  $\Phi_{DP}$  of fine scan is larger than that of coarse scan. In addition, there is no valid retrieval of total differential phase ( $\Phi_{DP}$ ) beyond 68 km away from the radar for the fine scan. From the plan position indicator (PPI) not shown here, it seems that radar radiation signal disappears entirely for the gates farther than 68km away from the radar for fine scan but not for coarse scan. The absence of  $\Phi_{DP}$  leads to infeasibility of attenuation correction at these gates. These differences of  $\Phi_{DP}$  can plausibly induce in the differences in the attenuation correction procedure.

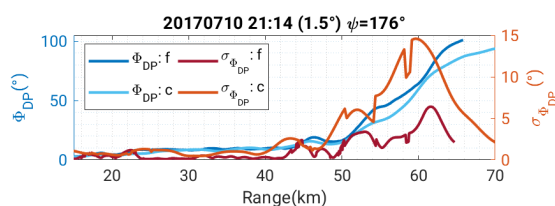


**Fig. 6** An example ray profile of total differential phase shift ( $\phi_{DP}$ ) and its radial texture at  $1.5^\circ$  elevation  $176^\circ$  azimuth at the 21:14UTC on July 10, 2017 through a wide-spread stratiform precipitation embedded with a few convective cells ( top: fine scan; bottom: coarse scan)

However, as illustrated in the Fig. 7, the radar reflectivity difference  $\Delta Z_H$  between the coarse and fine scan after attenuation correction fluctuates around an absolute value of 3dB. For the high reflectivity (larger than 45dBZ), 3dB difference will lead to considerably different estimates for instantaneous rainfall rate. As mentioned, severe attenuation of measurable signal leads to the absolute extinction of signal for the gates farther than 68km away from the radar exclusively for fine scan, which implies that the total measured  $\Phi_{DP}$  across the path are different for fine scan and coarse scan. As we know, the total measured  $\Phi_{DP}$  across the path serves as the constraint in the ZPHI attenuation correction procedure. Therefore, we can expect the different performance of attenuation correction for different spatial resolutions.

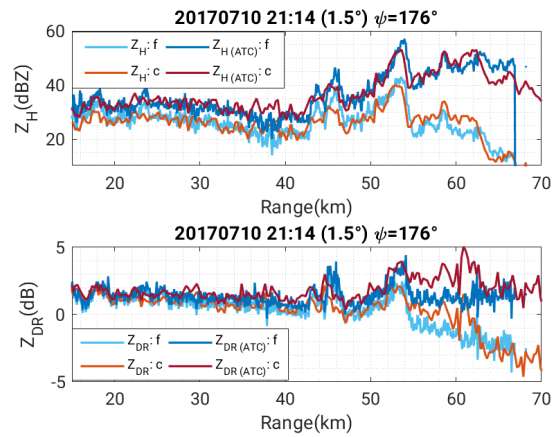


**Fig. 7** The same example ray as Fig. 6, but for the radar reflectivity and differential radar reflectivity before and after attenuation correction for both fine scan and coarse scan

To clarify, the manner of calculating radial texture in Fig. 6 is slight different from that in session 3.3. The retrieval of specific differential phase ( $K_{DP}$ ) uses the flexible number of consecutive gates conditioned by the radar reflectivity at that gate. The higher the radar reflectivity is, the less the gates will be involved in the retrieval of  $K_{DP}$ . To align with the retrieval of  $K_{DP}$ , the calculation of the radial texture of  $\phi_{DP}$  in 3.4 also adopts the changing radial lengths based on the magnitude of radar reflectivity, differing from the fixed radial lengths used in session 3.3. From Fig. 6, we can easily recognize that the texture of  $\Phi_{DP}$  from coarse scan can be three times larger than that of fine scan. Given the same number of gates, the length of range used for calculating the texture for coarse scan is also three times longer, which is inherently accomplished by a larger variability. That can explain why the magnitude of  $\Phi_{DP}$  in Fig. 4 is significantly lower than that of  $\Phi_{DP}$  from other radars.

### 3.5 Processed Data

The data directly acquired for radar volumetric scans (uncorrected radar reflectivity, unfiltered total differential phase shift, etc.) and the first-level products (corrected radar reflectivity and specific differential phase), are referred as 'raw' data here. The data processed additionally by the procedures such as the non-precipitating echo filtering and attenuation correction (ATC) is referred as 'processed' data. We mainly consider two procedures to process the data to achieve better data quality. One is attenuation correction that has been mentioned in 3.4. Another procedure is the non-precipitating echo filter that combines a 'good data' mask (Gematronik, 2007) and the meteorological index (Krause, 2016).

As revealed in the top plot in the Fig. 8, attenuation correction does not affect the  $Z_H$  measurements whose magnitude is lower than 0dBZ, but evidently increases the rest of  $Z_H$  measurements, especially larger than 18dBZ, to the higher values, suggested by a shift of the distribution curve from left to the right.

The bottom right plot in the Fig. 8 considers solely the measurement during the non-rainy period. It is obvious that the non-precipitating echoes filtering removes the most  $Z_H$  lower than 0dBZ, but maintains the rest  $Z_H$ . Before applying the non-precipitating echoes filtering, the fine scan provides a much lower probability of  $Z_H$  being -20 to 0 dBZ than that of coarse scan. Even for the  $Z_H$  after being processed with the non-precipitating echoes filtering, as shown in the bottom left plot in Fig. 8, the coarse scan is characterized by a higher probability of data between -20 and 12 dBZ. Regardless the non-precipitation echoes filtering, the fine scan with shorter pulse duration tends to lose the weak signals which are usually related to the non-precipitating echoes or the weak precipitation. Since the modest-to-heavy precipitation is our main concern, the absence of the unimportant radar reflectivity is not that problematic. However, in some special scenarios, for example, using the polarimetric measurements in the light rain to calibrate the differential radar reflectivity  $Z_{DR}$  or to monitor the radar performance, or retrieval of long-term precipitation climatology, we need to be cautious about this 'sacrifice' of losing weak radar reflectivity accompanied by higher resolutions. Besides the reduced amount of weak radar reflectivity, we also notice a shift between probability curves of fine scan and coarse scan for  $Z_H$  higher than 15 dBZ in the bottom left plot in Fig. 8. This shift means that the fine scan tends to be a few dB higher than the coarse scan, which  $Z_H$  calibration will account for, and the discussion of calibration will be in 4.1.

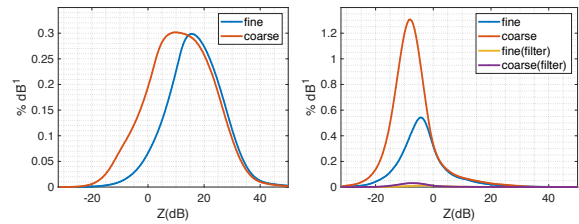
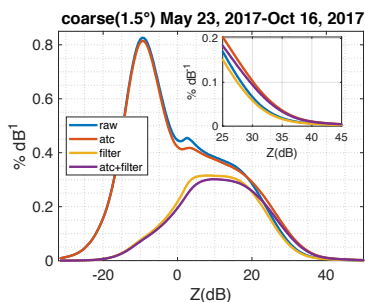


**Fig. 8** Probability density distribution function (PDF) of the radar reflectivity  $Z_H$ : the top is for coarse scan, where the blue line is the 'raw' data without being processed by attenuation correction (ATC) and non-precipitation echoes filtering, and the purple lines indicate the data processed by both procedures; the bottom left one shows the comparison of the 'processed' data between the fine scan and coarse scan; the bottom right one is exclusively for the data collected during non-rainy period

### 3.6 Data Quality for Dual-Polarization Quantities

Accessibility of the vertical-pointing scan in coarse scan provides us the chance to calibrate the differential radar reflectivity ( $Z_{DR}$ ). An offset of +0.8dB is determined from the probability density distribution (not shown) of the  $Z_{DR}$  data from in the 90° elevation scan. Due to the lack of vertical-pointing scan for the fine scan, we assume the offset of  $Z_{DR}$  obtained based on the coarse scan data is identical for fine scan as well, and this assumption could be invalid.

Fig. 9 shows the statistics of dual-polarization quantities from 24 light rain events occurring above the radar site. To guarantee the sample representativeness, each light rain event has the large and approximately similar amount of valid gates (~14500). Fig. 9 shows that the standard deviation of copolar correlation coefficient is lower than 0.01 in the light rain medium, and the averaged absolute deviation of ZDR is below 0.2dB. However, the medium and standard deviation of KDP is larger than the corresponding thresholds based on the S-band radar measurements from Marks (2011), which fits with the theoretically increased sensitivity of  $K_{DP}$  for the radars of the shorter wavelength.

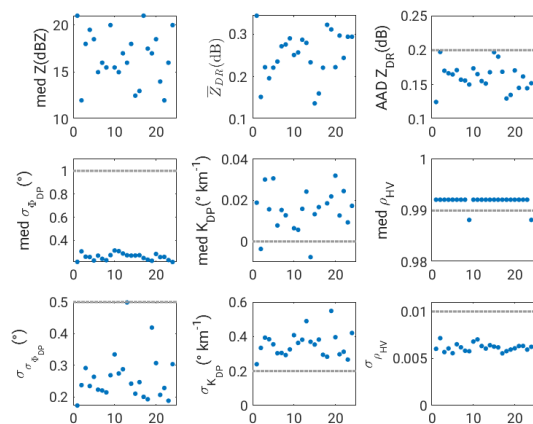


**Fig. 9** Statistics of dual-polarization quantities in the light rain event, including the averaged absolute deviation (AAD) for  $Z_{DR}$ , median and standard deviation of the texture of  $\Phi_{DP}$ ,  $K_{DP}$  and  $\rho_{HV}$ , where

the gray line indicates the threshold for qualifying the dual-polarization quantities according to Marks (2011)

## 4 APPLICATIONS

### 4.1 R-G Comparison

After applying the non-precipitating filtering and attenuation correction to the radar reflectivity, we retrieve the radar reflectivity ( $Z_H$ )-based precipitation estimates at two temporal resolutions, hourly and daily, and then compare the radar-retrieved precipitation estimates with the surface precipitation measurement from rain gauge network. However, the precipitation estimates from radar measurements still show noticeable underestimation when comparing to the ground reference measurements. This underestimation can be attributed to the lack of radar calibration. Thus, we then calibrate the radar measurement respectively for fine scan and coarse scan based on the comparison of the accumulative precipitation between the radar and rain gauge measurements for the whole experiment period, as revealed in Fig. 10. We allow the calibration factors to be different for fine scan and coarse scan, but we assume they are constant for all the rain gauges during the whole experiment period, regardless the range degradation of radar measurement and spatiotemporal variability of raindrop size distribution. For a single rain gauge station, the accumulative precipitation from rain gauge measurements is closest to the accumulative precipitation from radar reflectivity calibrated with 2dB, as illustrated in Fig. 10. Similar procedure is applied to the coarse scan. We are end up with two constant calibration factors, respectively for fine scan and coarse scan.

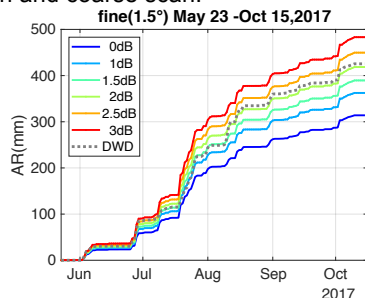


**Fig. 10** Rain accumulation of radar estimates with different calibration factor  $\Delta Z_H$  and rain gauge measurement (DWD) for a specific rain gauge station

After calibrating the radar reflectivity, quantitative precipitation estimates for fine scan and coarse scan can be retrieved respectively. The  $Z_H$  calibration does not increase the correlation coefficient, but significantly reduce the deviation between the radar estimates and rain gauge measurements. As illustrated in Fig. 11, precipitation estimates from both fine scan and coarse scan show good correlations with the rain gauge measurements. Furthermore, the statistics such as the correlation coefficient, the averaged absolute deviation, and relative root mean square error from the fine scan data demonstrate a slight better correlation between the radar estimates and rain gauge measurements. The radar-gauge comparison here is to use only one radar gate closest to the rain gauge station, instead of using an average

of 3×3 gates close to the rain gauge station. The small resolution volume of fine scan can provide the observation/resolution volume of precipitation closest to the rain gauge, to reduce the vulnerability of R-G comparison to the spatial variability of precipitation.

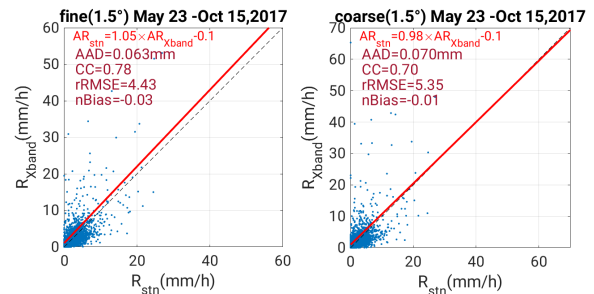


**Fig. 11** The comparison of hourly rain accumulation between the radar precipitation estimation and the rain gauge measurements, where AAD represents the averaged absolute difference, CC is the Pearson correlation coefficient, rRMSE means relative root mean square error, nBias indicates the normalized bias, and the equations are the least square fitting based on the minimum orthogonal distance to the fitting line

### 4.2 Quantitative Precipitation Estimation

In order to compare the difference of quantitative precipitation estimate directly between the fine scan and coarse scan, we interpolate the fine scan into the same spatial resolution as coarse scan and also interpolate the coarse scan into the same spatial resolution as fine scan. The first interpolation provides fine scan data in the resolution which is referred as f2c. The difference in rainfall rate estimated from f2c data and the coarse scan data is shown in the left plot of Fig. 12. Corresponding to this upscale procedure for the fine scan, a downscale procedure is applied to the coarse scan as seen in the right plot of Fig. 12. Clearly, the left plot is a smoothed version of the right plot, indicating that there is no abrupt disagreement between the fine scan and coarse scan. The noise filtering in 3.1 has already removed the noise of fine scan. The noise left by the noise filtering of SQI, if it exist, may be comparable to the noise in the coarse scan, and so we did not see the further noise inherently brought about by the fine scan.

Comparing the left and right plots in Fig. 12, we can find that the fine scan provides a more detailed spatial distribution of precipitation. For example, for the gate within the azimuth of  $314^\circ$  around 28km away from the radar, there is a local maximum of rainfall difference. Whether such additional details only visible by the fine scan, such as this aforementioned subtle structure is redundant or in demand depends on the purpose of application. For the extremely high hydrological forecasting for reservoir with complex topographic characteristics, or for the evaluating the extremely high-resolution land surface model, this finer information from the higher-resolution radar measurement can be necessary and desirable.

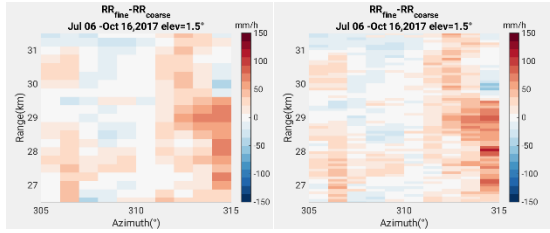


**Fig. 12** Difference of precipitation estimated from the fine scan and coarse scan with two interpolations of different spatial resolutions, where the left one is in framework of the resolution of coarse scan, the right one is for the fine scan

### 4.3 Hail Detection

Dual-polarization quantities provide further information regarding the size, phase and shape of the atmospheric hydrometers. For example, the dry hails usually exhibit extremely high radar reflectivity but near-zero differential radar reflectivity, which is quite different from the polarimetric characteristics of the normal large rain drops that have both high  $Z_H$  and  $Z_{DR}$ . With utilization of the polarimetric feature of hail, we attempt to identify the gates potentially containing the hail, as seen in Fig. 13. A supercell moved across the Stuttgart city area in the early afternoon on August 15, 2019 with hail reports from the European Severe Weather Database. Given the large supercell structure, we infer that hails were mostly mixed with liquid rain, so  $Z_{DR}$  is not necessarily closer to zero. We use the empirical relations between  $Z_H$  and  $Z_{DR}$  from Park (2008) to constrain the upper and lower threshold of  $Z_{DR}$  values according to the magnitude of radar reflectivity. The area of large hail potential, shown in the bottom row of Fig. 13, identified by the fine scan is slightly larger than that of coarse scan. The south area with high hail potential actually has not valid measurement of  $Z_{DR}$  before attenuation correction (not shown), which means that very few gates are identified as high hail potential before attenuation correction. It poses a prerequisite that the attenuation correction for  $Z_{DR}$  should be accurate enough to allow the hail detection to be reasonable and acceptable. In consequence, it is hard to determine the ability of fine and coarse scan in detecting hails because this detectability is considerably subjected to the accuracy of  $Z_{DR}$  or more precisely the correction for the differential attenuation.

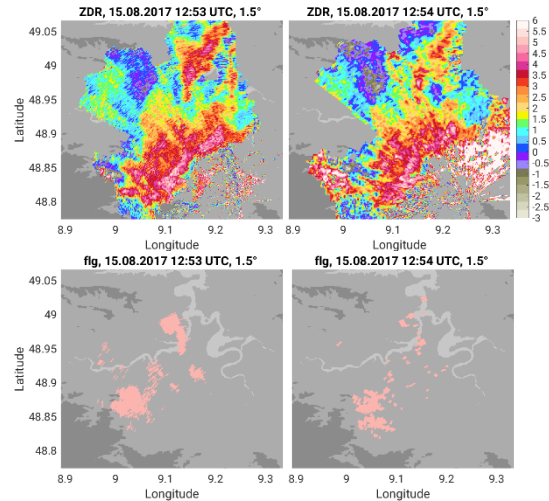
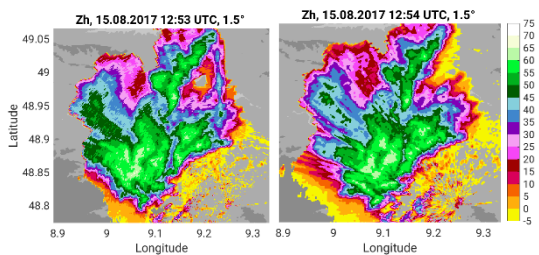


**Fig. 13** Radar reflectivity  $Z_H$  and differential radar reflectivity  $Z_{DR}$ , and hail flag for a supercell at 15:00UTC on August 15, 2017. Hails were reported by the European Severe Weather database during this supercell event (left column for fine scan, and right column for the coarse scan, and the top row for  $Z_H$ , the second row for  $Z_{DR}$ , and the bottom row for hail detection flag)

### 4.4 Convective Storm Tracking

The convective storm (CS) tracking algorithm named as *trace.3d* from Handwerker (2002) utilizes primarily the radar reflectivity measurement. Applying this tracking procedure to both the fine and coarse scan for the entire experiment period, statistical analyses of the variables characterizing the CS such the area, volume, mean rainfall rate, liquid water content and total water mass of all the detected convective storms is presented in the Fig. 14. This tracking algorithm does not distinguish whether the convective storm is short-lived or lasts for a few hours. This algorithm simply counts the number of observations of CS within the radar coverage during a predetermined time interval, and does not provide information of the actual number of convective systems over their entire lifespan. It means that one long-lasting convective storm can be counted twice or more during the consecutive time intervals. The time interval chosen here is 10-minute, corresponding to the temporal resolution of coarse scan. Since the temporal resolution of fine scan is not uniform, we decide to apply the tracking algorithm individually for the first, the second, and the third fine scan within each 10-minute radar-scanning period. As we know, most of convective storms have relative short lifespan, and the more transient the convective storm is, the smaller-scaled the convective storm may be. Therefore, counting the observation of CS is reasonable and can provide explicit information of frequency of occurrence of CS and implicit information of the development of CS.

As revealed in Fig. 14, the coarse scan provides a larger number of convective storms especially for the storms whose area is larger than  $6\text{km}^2$ , whose volume is larger greater than  $6\text{km}^3$ , and whose liquid water mass is greater than 3kilotons. It implies that the size of convective systems, which are not that small, becomes larger in the 'eye' of the coarse scan. It is

partially reasonable because the resolution volume of coarse scan is three times larger. For the coarse scan, the resolution volume of gates along the outer surface of the convective system will provide a larger volume for the entire convective storms.

One explanation for the smaller size of convective system seen by the fine scan data is that the *trace.3d* CS tracking algorithm used here was originally designed for the 500m-resolution C-band radar measurements with 14 elevations up to 30°. For the radar data having much higher resolution rather than 500m-resolution, the tracking procedure might omit some very small-scale precipitation systems which are actually detected by the radar data but not by the tracking algorithm. In addition, we only use the lowest three elevations of the volume scan for the coarse scan, to align with the fine scan. However, we know that convective storms often develop vigorously in the vertical direction. Only using the low elevation scans lower than 7° might not be able to depict the vertical extent of some full developed convective systems. After recognizing the potential inappropriateness of CS tracking algorithm, the *trace.3d* needs to be adjusted properly to be in accord with the radar measurement with high resolution, which could be a next step in this study.

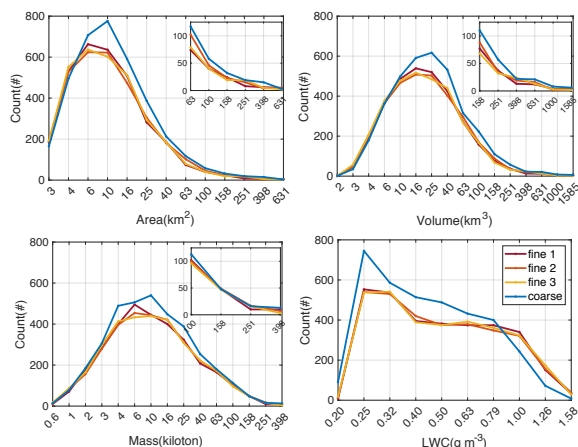


Fig. 14. Frequency of observations of convective storms from both fine scan and coarse scan, where the three fine scan tracking results are from the first, the second, and the third fine with each 10-minute interval

## 5. SUMMARY

We compare the radar data of two spatial resolutions, 'fine' scan and 'coarse' scan in terms of the data quality and the applications of radar data. Radar measurements with a higher spatial resolution tend to miss weak signals and have difference performance in static ground clutter identification, non-precipitating echoes filtering, and attenuation correction. Besides, the radar data with a higher spatial resolution agrees better to the surface rain

gauge measurement and provides more detailed information of precipitation at finer spatial structure. However, the advantage of using higher-resolution measurement for tracking convective storms and detecting hails is not clear yet and more analyses needs to be done before confirming the possible advantage.

## 6. REFERENCES

- Dufton, D.R.L. and Collier, C.G., 2015. Fuzzy logic filtering of radar reflectivity to remove non-meteorological echoes using dual polarization radar moments. *Atmospheric Measurement Techniques*, 8(10), pp.3985-4000.
- Gematronik 2007. Dual-polarization weather radar handbook, 2nd edition, V.N.Bringi, M.Thurai, R. Hannedsen(Ed.). Selex-SI Gematronik, 163pp
- Handwerker, J., 2002. Cell tracking with TRACE3D—A new algorithm. *Atmospheric Research*, 61(1), pp.15-34.
- Krause, J.M., 2016. A simple algorithm to discriminate between meteorological and nonmeteorological radar echoes. *Journal of Atmospheric and Oceanic Technology*, 33(9), pp.1875-1885.
- Marks, D.A., Wolff, D.B., Carey, L.D. and Tokay, A., 2011. Quality control and calibration of the dual-polarization radar at Kwajalein, RMI. *Journal of Atmospheric and Oceanic Technology*, 28(2), pp.181-196.
- Matrosov, S.Y., 2010. Evaluating polarimetric X-band radar rainfall estimators during HMT. *Journal of Atmospheric and Oceanic Technology*, 27(1), pp.122-134.
- Park, H.S., Ryzhkov, A.V., Zrníc, D.S. and Kim, K.E., 2009. The hydrometeor classification algorithm for the polarimetric WSR-88D: Description and application to an MCS. *Weather and Forecasting*, 24(3), pp.730-748.